npj | natural hazards

Article

https://doi.org/10.1038/s44304-026-00182-y

Monitoring landslide disturbances using distributed acoustic sensing under extreme weather conditions

Check for updates

Chengyuan Zhu[1], Yiyuan Yang[2], Kaixiang Yang[3] ✉, Weiqiang Zhu[4] & Qinmin Yang[5] ✉

Extreme weather significantly challenges the effective and timely monitoring of landslide disasters. Distributed acoustic sensing (DAS) offers unique capabilities for monitoring slope failures during extreme weather events such as typhoons by transforming pre-deployed optical fiber cables into high-resolution vibration-acoustic sensor arrays. This study documents sudden shifts in landslide disturbance signals during a super typhoon's passage using DAS with 1 Hz downsampled modulated signals. By leveraging multi-domain analysis (time-frequency-space), we identify landslide disturbance micro-deformation signatures, revealing interconnected spatial responses and dynamic patterns. We introduce a spatiotemporal indicator evaluation framework to monitor landslide occurrence and evolution under extreme weather conditions. The monitoring of landslide occurrence correlates well with post-disaster incident records and meteorological data. These results demonstrate that DAS systems can enhance early detection and high-resolution monitoring of landslide disasters under extreme weather conditions, highlighting the potential for comprehensive natural disaster management.

Landslides triggered by extreme weather events, particularly typhoon-induced rainfall, represent a formidable challenge worldwide, causing extensive human casualties and economic losses of over $20 billion annually[1–3]. For instance, Typhoon Mangkhut (2018) struck Southeast Asia and triggered catastrophic landslides in the Philippines, which led to over 100 deaths and displaced thousands of individuals. Similarly, Typhoon Rai (2021) induced severe landslides in the Philippines, exacerbating socio-economic burdens on affected communities[4,5]. These extreme events increase the likelihood of sudden, large-scale slope failures, complicating the monitoring and early warning of landslides[6–8]. The inherent unpredictability and rapid development of such disasters present a formidable challenge for effective monitoring and disaster mitigation.

Despite advancements in monitoring technologies, existing methods continue to face significant limitations during extreme weather conditions. Satellite remote sensing, while providing large-scale spatial coverage, often suffers from compromised accuracy and reduced real-time performance due to intense rainfall and dense cloud cover, rendering it less effective when monitoring is most critical[9–13]. Traditional geological hazard monitoring systems, such as radar and optical technologies, have been extensively deployed to track surface deformation and landslide activity. Ground-based instrumentation, such as inclinometers and piezometers, although highly accurate at specific locations, presents deployment challenges in remote or typhoon-prone terrains and is typically limited to monitoring deep, slow-moving landslides[14–16]. Geophysical methods (e.g., using seismic networks) have demonstrated utility for monitoring sub-surface activity, but their deployment is constrained by high deployment costs and continuity challenges in maintaining dense sensor network[17–20]. Distributed acoustic sensing (DAS) presents distinct advantages in the domain of landslide monitoring compared to traditional monitoring technologies[21–23]. DAS leverages existing optical fiber cables to function as continuous, extensive seismo-acoustic arrays capable of detecting minute subsurface movements with high spatial resolution up to 100 km[24,25]. For example, Lindsey et al. applied DAS to convert a submarine cable into a 20-km-long seismic array for ocean observation, successfully identifying multiple submarine fault zones and tracking sea state dynamics during the North Pacific storm cycle[26]. Zhu et al. developed a deep learning model for DAS data processing to enhance earthquake detection and phase picking, achieving better accuracy and efficiency than conventional approaches by detecting more subtle seismic events[27–29]. This capability allows DAS to provide near-real-time strain measurements, essential for identifying subtle pre-failure signs of

[1]College of Control Science and Engineering, Zhejiang University, Hangzhou, Zhejiang, China. [2]Department of Computer Science, University of Oxford, Oxford, Oxfordshire, UK. [3]College of Computer Science and Engineering, South China University of Technology, Guangzhou, Guangdong, China. [4]Department of Earth and Planetary Science, University of California, Berkeley, Berkeley, CA, USA. [5]State Key Laboratory of Industrial Control Technology, College of Control Science and Engineering, Zhejiang University, Hangzhou, China. ✉e-mail: yangkaixiang@zju.edu.cn; qmyang@zju.edu.cn

landslides and tracking progressive deformation patterns induced by extreme weather events. Lin et al.[4] demonstrated the innovative application of DAS with submarine optical-fiber cables for real-time ocean monitoring during typhoons, observing microseismic noise induced by ocean surface gravity waves (OSGWs) and successfully mapping OSGW propagation along a submarine optical-fiber cable using frequency-wavenumber analysis. Their approach confirmed the effectiveness of DAS for continuous, high-resolution monitoring of ocean conditions under typhoon scenarios. Moreover, DAS delivers rich, continuous data streams that capture both transient and progressive deformation, enabling comprehensive risk profiling and supporting proactive disaster response. Ouellet et al.[30] demonstrated the use of DAS for high-resolution landslide monitoring, capturing sub-millimeter displacements and strain-rate changes that conventional methods could not detect. This high-resolution data not only tracks the subtle evolution of landslide activity but also provides crucial information for early warning systems and disaster mitigation. Michlmayr et al.[21] utilized fiber-optic cables for high-resolution acoustic emission (AE) monitoring of slope failure mechanisms. Extensive and long-term deformation monitoring can help identify deformation anomalies preceding failure, thereby enhancing prediction and warning capabilities[31]. However, despite the advancements in DAS technology, current research has not yet effectively leveraged DAS for monitoring landslide disturbances under extreme weather conditions. There remains a gap in the comprehensive analysis of monitoring data, limiting the full potential of DAS in such scenarios[32,33]. Further exploration of how DAS systems can be optimized for monitoring slope failures during extreme weather events is crucial, and assessing the role of DAS in these contexts remains a critical area for future research.

This study investigates the application of pre-deployed DAS systems to detect and characterize sudden changes in landslide disturbance signals during the passage of a super typhoon across complex mountainous terrain. Our findings demonstrate that buried DAS cables effectively capture micro-deformation noise induced by the typhoon, revealing interconnected and expansive spatial responses. Furthermore, we introduce a novel approach for monitoring landslide hazards during extreme weather events based on key indicator analysis derived from DAS measurements. This method, supported by three critical indicators, successfully reveals the relationship between environmental disturbances and landslide occurrences, offering high-resolution insights into the dynamic effects of extreme weather on landslide stability processes.

Results

DAS system and geographical environment overview

The deployed DAS system utilized in this study is an emerging sensing technology based on phase-sensitive optical time-domain reflectometry (ϕ-OTDR) technology, which exploits the high sensitivity of coherent Rayleigh backscattering in optical fibers to detect environmental vibrations and acoustic fields with remarkable spatiotemporal resolution (Supplementary Fig. S1)[34–36]. The system was independently developed and deployed by our research team, with comprehensive system specifications detailed in Supplementary Table 1. The DAS system typically operates with dual channels, connecting the fiber optic cable bidirectionally as Channel 1 and Channel 2. Channel 1 and Channel 2 each include 1 to 960 channels, denoted as channel $i - j$, where i is 1 or 2, and j is 1 to 960. Initially developed for monitoring the safety of oil and gas pipelines within the smart pipeline infrastructure networks of Zhejiang Province, the DAS system oversees over 2000 km of critical infrastructure. The optical fiber cable network installed in 2019 spans diverse terrains, including complex mountainous regions and densely populated urban areas. Deployment in such varied environments presented significant engineering challenges, particularly in the mountainous zones where cable burial had to balance depth for protection against shallow landslides and rockfalls with the need to maintain adequate coupling with the surrounding soil to detect strain effectively. To achieve effective ground coupling necessary for geophysical sensing, the cable was typically trenched to a depth of approximately 1 m and backfilled with native soil, ensuring intimate contact with the surrounding earth. This direct burial method enhances the cable's sensitivity to soil strain, as opposed to being loosely laid in a conduit, which can decouple the fiber from small ground deformations. These considerations directly impact long-term maintenance, as a well-coupled and protected cable reduces the risk of damage and signal degradation, extending the system's operational lifespan with minimal intervention. For security reasons, the precise layout of the network is not disclosed; however, a specific 50-km segment relevant to this study is depicted in Fig. 1. This segment represents a portion of the system's full monitoring capability, which extends up to 100 km per interrogator unit. The system operates continuously with a spatial resolution of 50 m and a sampling frequency of 2 kHz. Raw phase data recorded by the DAS system are processed into strain rate measurements at a temporal resolution of 1 Hz for subsequent analyses (see "Methods" for details on raw data processing). This downsampling to 1 Hz for analysis is a key factor in enabling practical system operation. It focuses on the low-frequency components most relevant to landslide-scale ground deformation, dramatically reduces the computational burden and data volume for real-time processing and transfer, and aligns with the typical minute-to-hour temporal evolution of landslide precursors, making it suitable for operational monitoring and early warning. In terms of cost and power, the system's reliance on a single device per 100 km segment, coupled with efficient data reduction, results in a favorable profile compared to dense networks of traditional sensors, with power consumption primarily driven by the device unit itself, often compatible with the power supply equipment in the pipeline station or valve chamber.

The geographical environment along the monitored optical fiber cable segment (Fig. 1a, blue circular line) is characterized by significant topographical variability. As shown in Fig. 1c, this region includes both mountainous terrains with landslide-prone zones reaching high elevations and flat urban plains spanning approximately 10 km. The fiber segment intersects both urban and rural areas, providing a unique opportunity to investigate environmental responses across diverse landscapes. Super Typhoon Muifa, one of the most intense typhoons to impact the region in recent decades, made landfall in Zhejiang Province, China, at 12:30 UTC on September 14, 2022. Figure 1a illustrates the typhoon's trajectory and the extent of its associated extreme weather conditions, based on satellite imagery provided by the China Meteorological Administration. Two landslide events confirmed by local authorities during the Typhoon Muifa are indicated in Fig. 1b by orange inverted triangles, located near the initiation points of DAS Channel 1 and Channel 2. These catastrophic failures caused the collapse of nearby road sections and exposed underground pipelines, as shown in Supplementary Fig. S2. The DAS system's capacity to capture micro-deformations associated with slope failures provides a unique advantage for landslides early warning and disaster assessment. This capability underscores its potential for rapid response in scenarios where conventional monitoring methods face limitations. Supplementary Fig. S3 shows the raw signal acquisition waveforms from the DAS system, illustrating the environmental vibrations and acoustic fields detected. The waveforms are characterized by high-frequency oscillations corresponding to the rapid changes in environmental conditions during the monitoring period. The DAS system has demonstrated unique capabilities in detecting and localizing landslide disturbances with fine temporal and spatial resolution during the extreme conditions brought about by Typhoon Muifa.

The data monitored by the DAS system play a crucial role in this study by providing high-resolution, continuous monitoring of landslide disturbances under challenging weather conditions. The system's ability to capture both transient and gradual ground movement allows for a comprehensive understanding of landslide behavior during extreme weather events. This high-resolution data is essential for developing early warning systems and improving disaster response strategies, as it facilitates the identification of critical warning signs and real-time tracking of landslide evolution. The DAS system's data also support the development of forecasting models for landslide events, potentially enhancing our

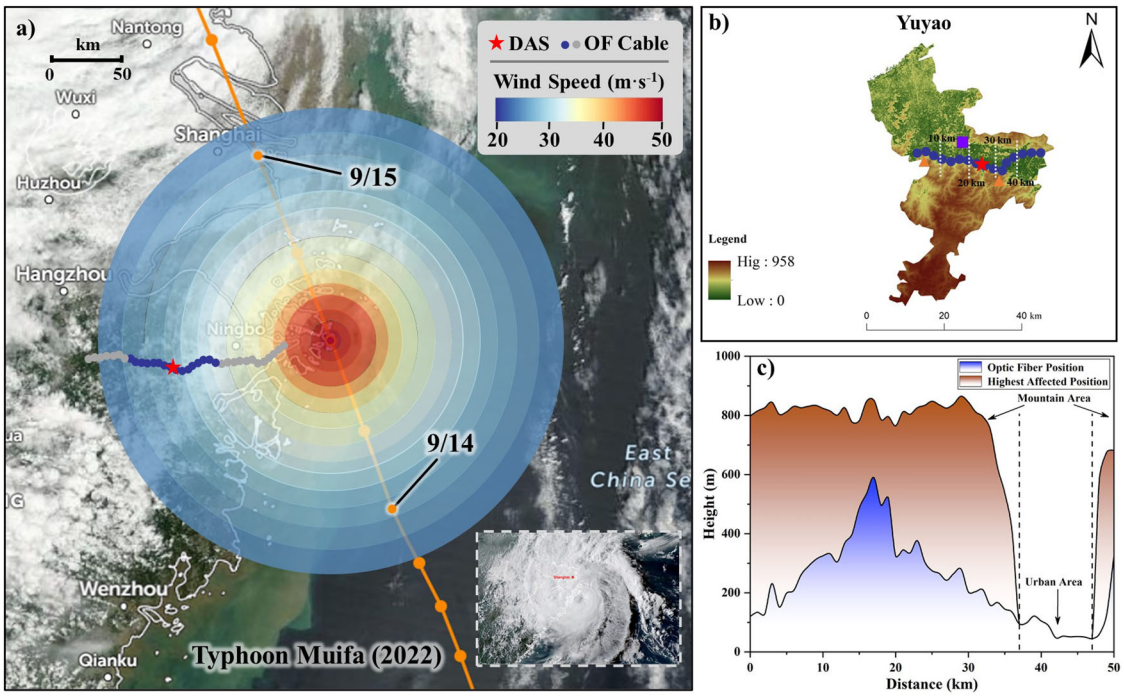

Fig. 1 | The deployment of distributed acoustic sensing system (DAS) during the impact of Typhoon Muifa. a Satellite images showing the impact range of Typhoon Muifa in Zhejiang, China from September 14th to 16th, 2022 (UTC). The concentric circle represents the range of wind impact intensity (drawn around the time of Typhoon landfall at 12:30 on September 14th). The red star indicates the location of the DAS interrogator location. Blue dots represent the monitored optical fiber cable segment (50 km), while gray dots represents unmonitored sections. **b** Topographical map of the monitoring area showing the optical fiber (OF) cables through the Yuyao City. The purple box represents the location of the weather station. The blue circular line represents OF cables, with a distance of 50 km, separated by gray dashed lines every 10km. The orange triangles mark the locations of two confirmed landslide locations corresponding to the channel positions in Fig. 2b, c. **c** Elevation profile along the optical fiber cable route revealing the transition from mountainous terrain in landslide-prone areas to urban plains.

ability to mitigate the impacts of landslides on human life and infrastructure.

Spatiotemporal representation of landslide disturbance propagation

To elucidate the propagation of landslide disturbance micro-deformation signatures during Typhoon Muifa, we generate distance-frequency spectrograms spanning September 14–16, 2022 (Fig. 2a). These micro-deformation signatures, captured by DAS systems in mountainous environments, encompass various vibration sources such as landslides, water flow, human activities, and other environmental vibrations. Micro-deformation noise specifically describes the deformation signals generated during the precursory phase of slope failures, containing unique vibration characteristics preceding slope instability. The micro-deformation signatures distinguish critical landslide precursors from generic environmental noise, enabling targeted analysis of geomechanical instability signals in DAS monitoring. These spectrograms capture the spatiotemporal dynamics of micro-deformation noise recorded by the DAS system across the monitored 50-km cable segment, revealing frequency energy intensity (0–0.5 Hz) distributions. The DAS system detects strain disturbances through optical phase changes (DAS_{phase})[37], which exhibit a linear relationship with strain rate (DAS_{ε}) and can be expressed as expressed as Eq. (1):

$$\mathbf{DAS}_{\varepsilon} = \frac{\lambda \mathbf{DAS}_{\mathbf{phase}}}{4\pi n l_g \xi} \tag{1}$$

where λ denotes the wavelength of the narrow-linewidth pulse, set to 1.55×10^{-6} m; n is the refractive index of the optical fiber, specified as 1.467; and l_g represents the gauge length, which determines the sensitivity of strain measurements. The strain-optical proportionality factor, ξ, is standardized at 0.78, as its temperature dependence is negligible under the studied conditions. Fourier transformation (FT) is employed to extract frequency-domain data for each monitoring channel across the observation window (September 14, 00:00 UTC, to September 16, 00:00 UTC). The DAS signal in the time domain is transformed into the frequency domain through FT to obtain the frequency-domain representation $X(f)$ of the signal. Then, the energy spectrum is calculated as $X(f)^2$, which indicates the energy distribution of the signal at different frequency components. Finally, the energy spectrum will be logarithmically transformed into decibels (dB), can be calculated as $P(f) = 10\lg|X(f)|^2$. This transformation helps in comparing and analyzing the relative energy of different frequency components more conveniently and provides a more intuitive representation of energy variations. While baseline energy spectrum remained low (< 0 dB) for most channels, two pronounced intensity surges (20–80 dB) have been detected, corresponding to confirmed landslide events. These disturbances predominantly occur in regions at elevations between 200–300 m, with the highest impact observed at locations of high topographical variability (Fig. 1c).

Figure 2b, c provide high-resolution time-frequency plots for two distinct landslide sites, revealing their temporal evolution and spatial characteristics. In Fig. 2b, channels 1-25-27 exhibit sustained high-frequency fluctuations over time, characterized by dense clusters of high-energy signals (indicated by yellow intensity). These patterns suggest repeated micro-deformations likely triggered by cascading impacts from unstable slopes at higher elevations. By contrast, Fig. 2c reveals abrupt and intense energy bursts (>50 dB) spanning three adjacent zones in Channel 2, peaking at approximately 11:00 UTC on September 14. This activity coincides with the passage of Typhoon Muifa, suggesting the storm's direct role in triggering slope failures between 10:00 and 15:00 on September 14th. The two sites display distinct temporal and spectral characteristics that align with the rapid deformation and sliding stage of landslides. The persistent deformations in Fig. 2b correspond to retrogressive failure within scarp zones, while the rapid, high-energy bursts in Fig. 2c indicate triggering zones

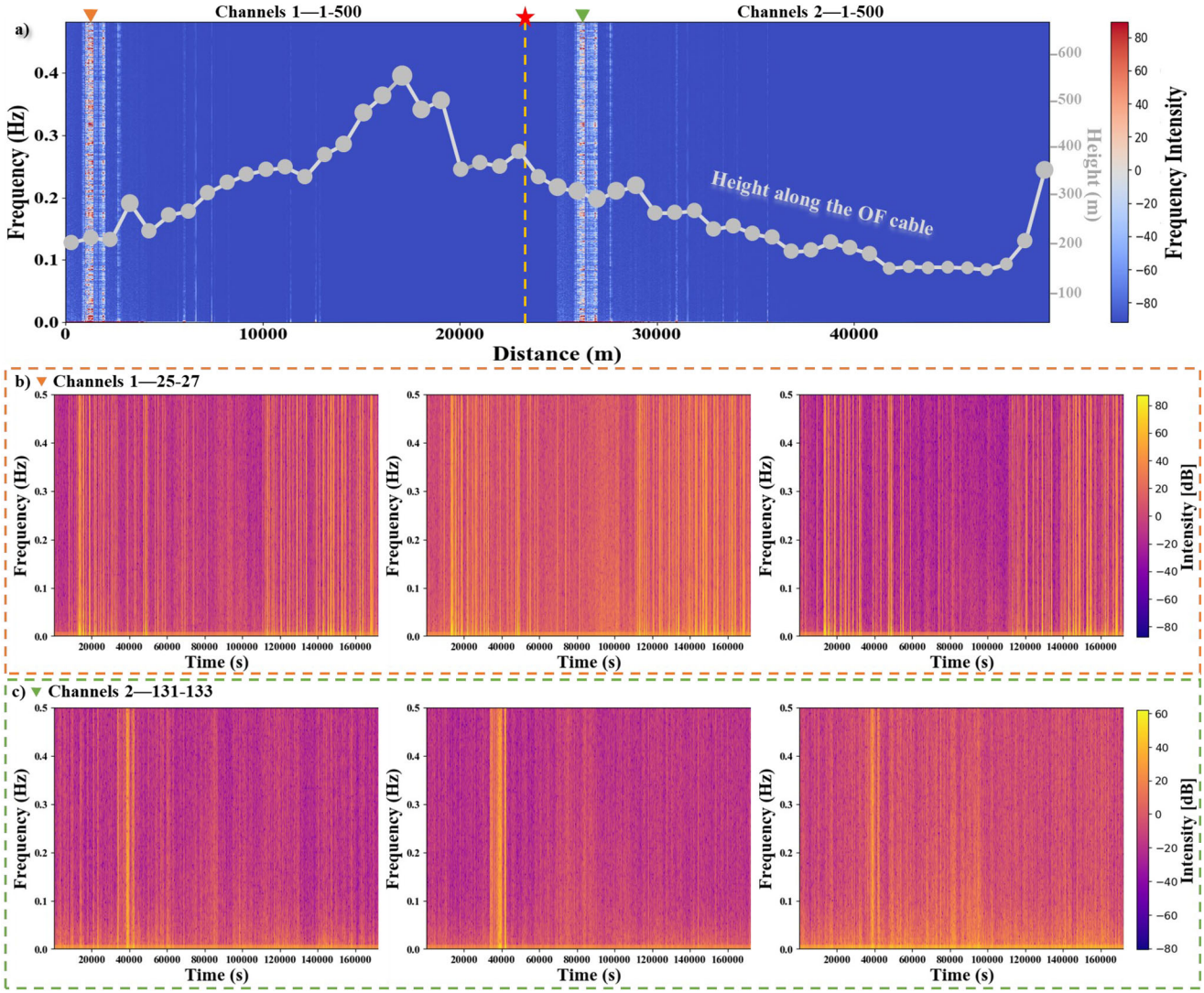

Fig. 2 | The spatial-temporal characteristics of micro-deformation signitures recorded by the DAS system during the passage of Typhoon Muifa. a The distance-frequency spectrogram showing energy distribution along fiber optical cable against elevation profile (gray line). The red asterisk represents the position of the DAS interrogator position at the monitoring area center with two channels in both directions. The orange and greeen inverted triangles represent the locations of two confirmed landslide locations, corresponding to the areas of channels 1–20 to 1–30 and channels 2–130 to 2–140, respectively. **b**, **c** show time-frequency spectrograms of the specific channels at the two landslide locations, covering September 14–16, 2022. The color of the time-frequency spectrogram represents the change in intensity levels.

associated with slope instability. These observed spatiotemporal features are consistent with the retrogressive scarp failure zone and the rapidly propagating triggering zone described in previous studies by Ouellet et al.[30] and Hu et al.[11]. Unlike conventional methods, the DAS system directly captures these signals from in situ deformation processes, demonstrating its ability to monitor disturbances in real time and with high granularity. Moreover, we observe that the micro-deformation signatures are influenced by meteorological factors such as rainfall, consistent with mechanisms underlying landslide initiation. The characteristics of this noise suggest complex interactions among multiple factors contributing to landslide dynamics under extreme weather conditions. By leveraging the DAS system's high temporal and spatial resolution, we provide new insights into the propagation of landslide disturbances, offering advancements for landslide monitoring, risk assessment, and early warning systems.

Multivariate analysis of landslide disturbance during Typhoon passage

To comprehensively characterize the impact of Typhoon Muifa on landslide-related disturbances, the S-transform analysis (detailed in "Methods") is applied to enhance signal characteristics, enabling an in-depth analysis of multivariate correlations with meteorological variables, including wind speed, relative humidity, and rainfall. Compared to remote sensing observations, the DAS observation after S-transform provides improved sensitivity to micro-terrain disturbances, capturing key signals in the 0.01–0.6 Hz frequency range within an intensity range of −120 to −100 dB. The time-frequency spectrograms derived from the S-transformation (Fig. 3a–f) illustrate the energy distribution of the signals. The red traces on the spectrograms indicate regions of heightened energy corresponding to the micro-deformation signatures.

The characterization of landslide features captured by DAS requires a combination of intensity changes, temporal persistence, and spatial propagation. Sudden anomalies alone are insufficient to distinguish landslide signals from other micro-deformation phenomena. For example, micro-deformation signatures are captured at the position in Fig. 3a–c, but no landslide is confirmed. Channel 1-009 exhibits localized and transient deformation without spatial continuity, indicating unrelated disturbances. Channel 1–131 displays weak and short-lived disturbances, while channel 1–259 shows low energy intensity, likely caused by minor soil loosening or

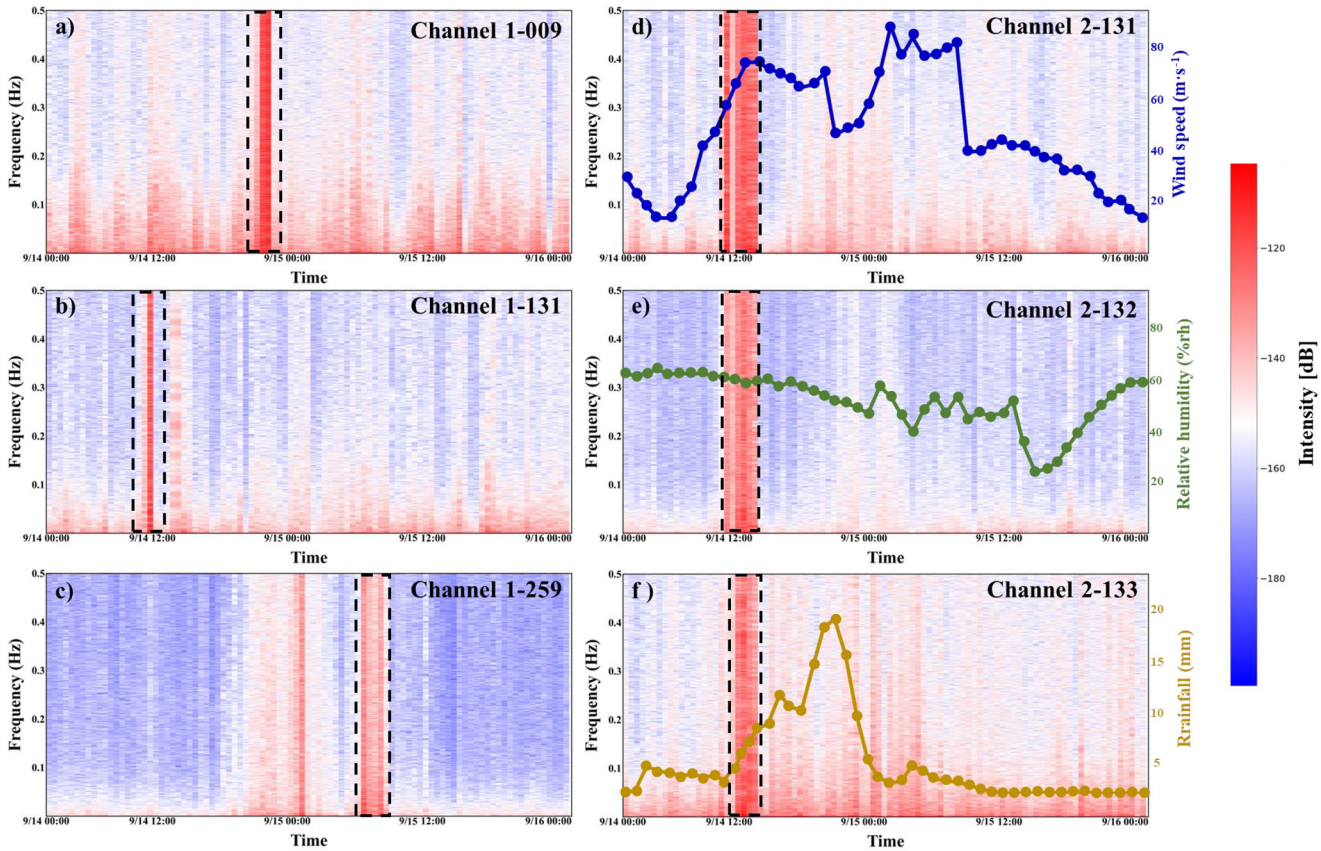

Fig. 3 | The time-frequency energy spectrum of DAS signals at confirmed landslide locations after S-transformation and relevant meteorological data during the extreme weather Typhoon Muifa. a–c Representative channels exhibiting micro-deformation noise without confirmed landslides. The black box represents the captured abrupt signals of disturbances. **d–f** Channels capturing confirmed landslide events with correlated meteorological data. Meteorological data of wind speed, relative humidity, rainfall records are represented by dashed lines with corresponding scales on the right axes of (**d–f**), respectively. textbf (**a**) represents the S-transform energy spectrum of channel 1-009, and the black box represents the captured abrupt signal of micro-deformation noise associated with slope failures in terrain (**b**) represents the S-transform energy spectrum of channel 1-131. **c** represents the S-transform energy spectrum of channel 1-259. The red cyan lines represent stronger energy fluctuations. Micro-deformation noises are captured at the position in (**a–c**), but no landslide is confirmed. **d–f** denotes the S-transform energy spectrum of channels 2-131 to 2-133, where the landslide location has been confirmed. The wind speed records in this area are marked in (**d**). The relative humidity of the area is marked in (**e**). Rainfall records are marked in (**f**).

water erosion. Vibrations induced by surface runoff or debris impact. Additionally, there are other environmental or anthropogenic noises unrelated to slope instability. In Supplementary Fig. S4, we present the time-frequency characteristics of typical channels after S-transformation, demonstrating that with appropriate processing, the DAS system can effectively highlight the features of vibration under extreme weather conditions. In contrast, Fig. 3d–f illustrate channels associated with confirmed landslide events, characterized by distinct signal features: sharp energy surges, sustained high-energy activity, and spatially coherent propagation. These characteristics align with landslide-specific strain dynamics[38], as captured by the DAS system detecting the interplay of geophysical forces and environmental conditions. By leveraging the DAS system's sensitivity to geophysical perturbations transmitted through optical fibers, we have identified significant strain anomalies across various channels over time. These anomalies evolve during the typhoon's passage and are correlated with changes in rainfall, wind speed, and humidity. The DAS system's ability to capture strain energy with sub-second resolution and meter-scale spatial resolution enables real-time monitoring of landslide disturbance processes. However, extreme weather conditions often amplify the frequency and scale of landslides while simultaneously hindering signal transmission and reception. These systems face operational challenges in complex terrain and incur high deployment and maintenance costs. Furthermore, their spatial and temporal resolutions are typically limited to kilometer-scale and hour-level granularity, respectively. In contrast, the DAS system's exceptional sensitivity to environmental changes enables the detection of subtle geological movements and acoustic variations, even under extreme weather conditions. In the following section, we propose a framework utilizing critical indicators to evaluate and characterize landslide hazards under extreme weather conditions. This approach holds promise for enhancing geological hazard early warning systems, particularly in the context of increasing extreme weather events driven by climate change. The framework offers the potential for more accurate regional landslide estimation and predictive modeling of their progression.

Indicators for landslide occurrence

To accurately identify landslide disturbances from DAS system signals, we develop a robust evaluation framework based on three critical indicators, including spectrum intensity gradient (SIG), duration (DUR), and radiation range (RAR). These indicators are designed to capture the signal's intensity variation, temporal persistence, and spatial propagation characteristics, respectively. By employing dual sliding windows in both time and space dimensions, the framework detects the potential signal evolution and utilizes a Gaussian decay model[39] to assess the relative importance of each indicator. Figure 4a, b illustrate spatiotemporal heatmaps of SIG across the first 200 channels in two monitored Channel 1 and Channel 2, revealing episodic clustered bursts of energy (marked with black boxes) during monitoring periods, which are strongly indicative of micro-deformation occurrence. In contrast, "quiet zones" exhibit stable signal patterns without

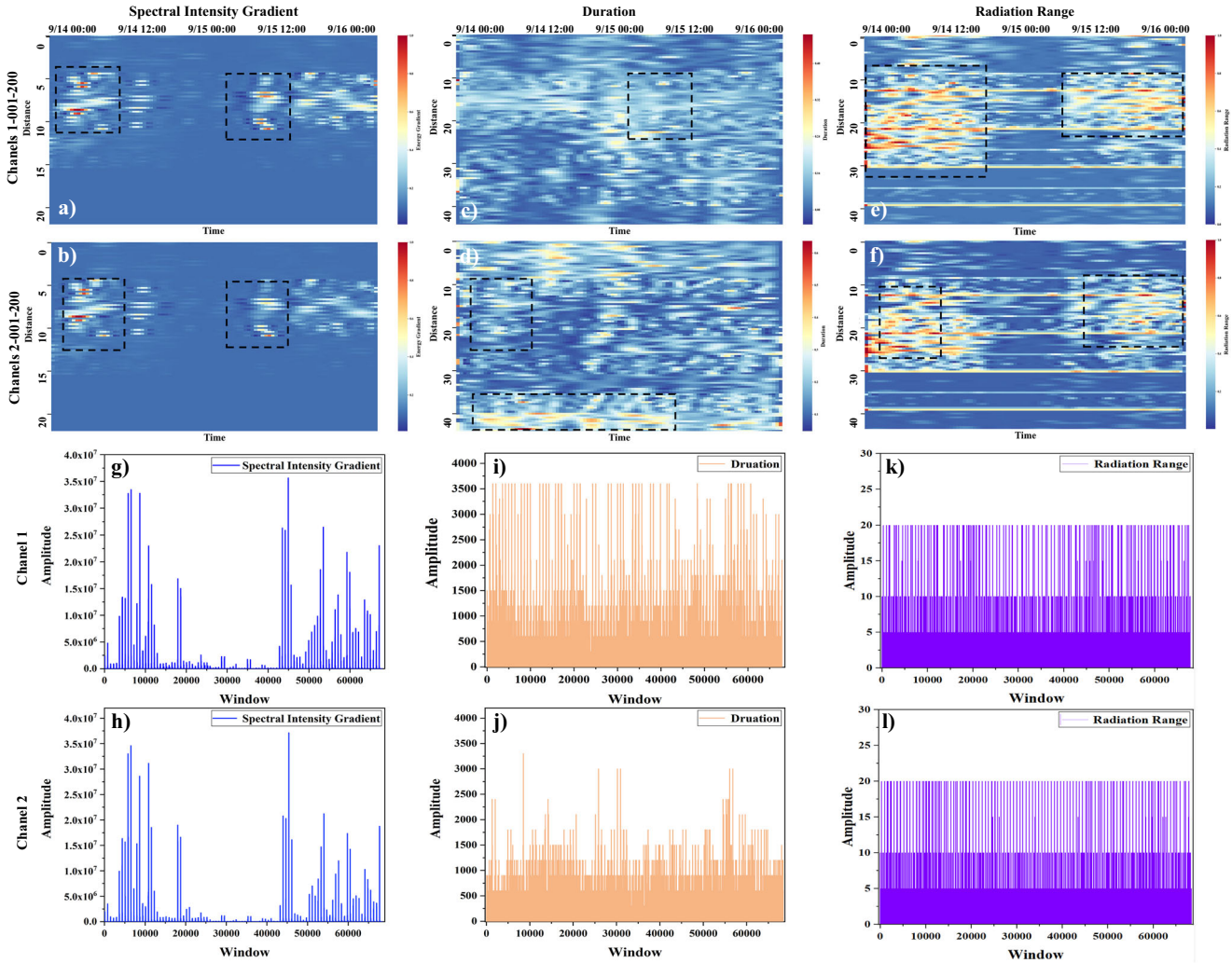

Fig. 4 | Critical indicators for landslide detection derived from DAS recording during Typhoon Muifa. Spatiotemporal heatmaps of three key indicators of spectrum intensity gradient (SIG) (**a**, **b**), duration (DUR) (**c**, **d**), and radiation range (RAR) (**e**, **f**). Color gradients from blue to red indicate increasing intensity. Black boxes highlight areas of significant micro-deformation signals corresponding to confirmed landslide locations in Fig. 2a. **g–l** Statistical distributions of indicator amplitudes across monitoring windows. The window is set based on the extraction range of indicators, with the two dimensions of time and space. **g**, **h** represent SIG amplitude variations directly correlating with disturbance magnitude. **i**, **j** represent DRU distributions showing sustained activity patterns with an interval range of 0–3600. **k**, **l** represent RAR distributions related to the spatial window with an interval range of 0–20.

steep gradients, clearly distinguishing them from burst zones. Window-based statistical analyses of SIG (Fig. 4g, h) further highlight its significant magnitude variations, which emerge as the most prominent hallmark of sudden disturbances. However, such abrupt changes may also originate from sporadic impacts or other external factors unrelated to landslide disturbance. To further refine disturbance assessments, we introduce sliding windows in both time and space dimensions to extract additional indicators. Figure 4c, d presents DUR heatmaps that quantify the temporal persistence of high-intensity signals. The Gaussian decay model effectively characterizes signal intensity over time, identifying regions of prolonged high-energy fluctuations (marked in black boxes), which underscore the persistence of energetic disturbances during extreme weather events. Similarly, the spatial propagation of disturbances is quantified by RAR (Fig. 4e, f), which measures the extent of signal diffusion from high-energy epicenters to adjacent zones. By analyzing the impact of high-energy regions on adjacent areas within the same time window, we identify two different, distinct patterns of strip-shaped and clustered distributions. The occurrence of landslide disturbance induces a cascading effect, where neighboring zones exhibit significant signal strength increases, as indicated by the aggregated heatmap clusters (black boxes). Figure 4i–l compares the statistical distribution of DUR and RAR across windows, revealing the differences between the two landslide events. In Channel 1, the landslide phase is characterized by sustained and widespread disturbances, with DUR and RAR exhibiting higher amplitudes and stronger persistence and propagation. Supplementary Fig. S5 shows that the statistical distribution of the two indicators for Channel 1 is also concentrated in the larger interval. In contrast, the event captured by Channel 2 is less pronounced, with only a few windows reaching higher levels, potentially reflecting a rapid landslide event. Fig. 5 provides a comprehensive assessment of the performance and fluctuation ranges of critical indicators for both Channel 1 and Channel 2. Figure 5a, b depict SIG variations over time, with the green solid lines representing the mean and the shaded areas indicating fluctuation ranges. These ranges are deviations, the deviation range of each channel from the mean at the same time. SIG exhibits significant oscillations at critical landslide time points (corresponding to around 10:00 on September 14th and 12:00 on September 15th), suggesting its sensitivity to sudden disturbances. DUR and RAR trends, as shown in Fig. 5c–f, display relatively smoother variations but still demonstrate notable deviations at key moments.

These visualized results demonstrate that the evaluation framework successfully identifies landslide disturbances under extreme weather conditions, with observed events localized within a 5–10 km range. These findings showcase the potential of DAS for real-time landslide monitoring

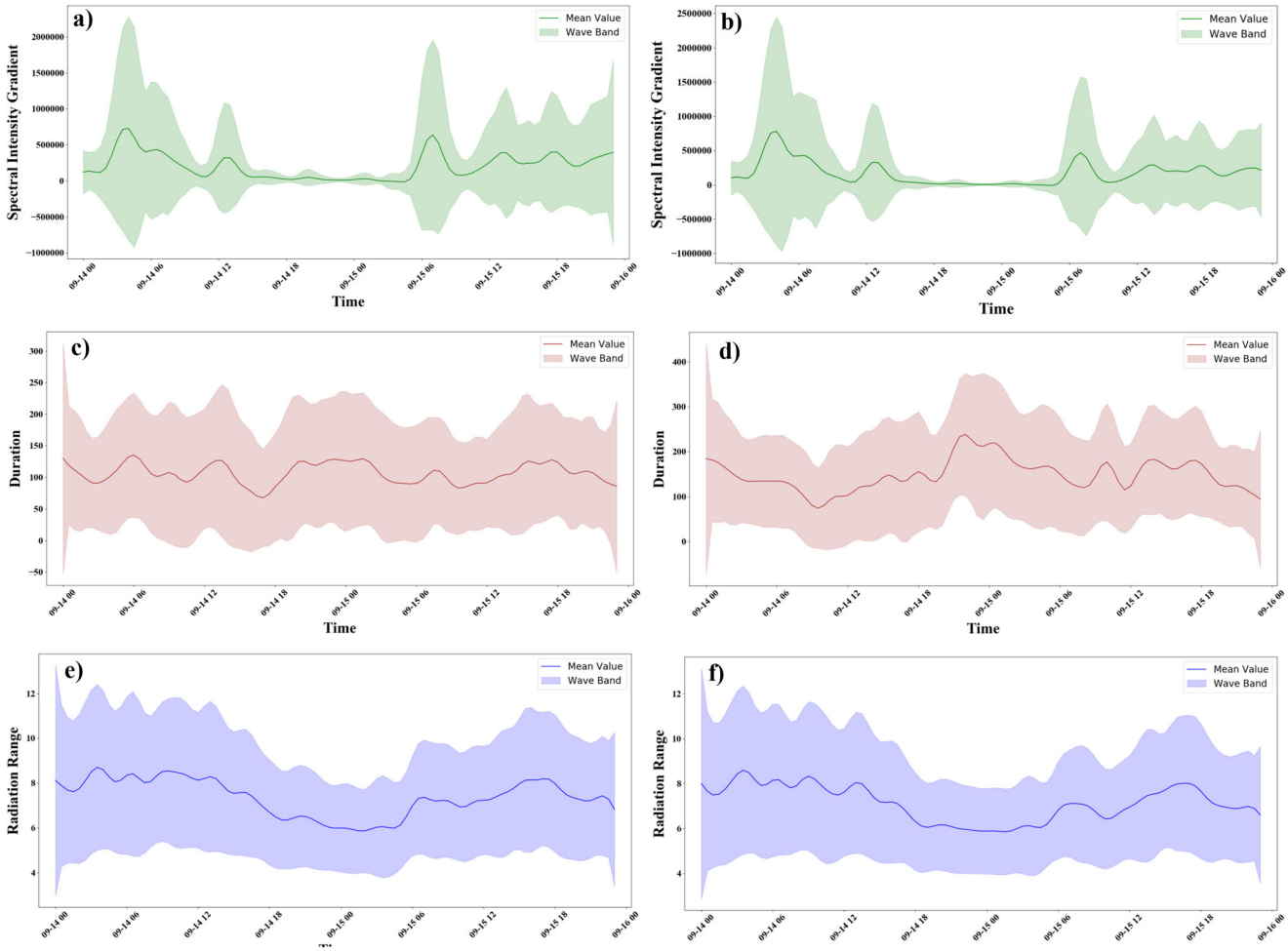

Fig. 5 | Temporal evolution and variability of critical indicators during Typhoon Muifa. The time series analysis of the three indicators is drawn at 1-s intervals. **a**–**f** shows temporal variations in spectrum intensity gradient (SIG), duration (DUR), and radiation range (RAR), respectively. Solid lines represent mean values while shaded areas indicate fluctuation ranges. **a**, **b** denote the level of change in the spectrum intensity gradient (SIG) indicator. The green solid line represents the mean value of SIG over time, and the green area represents the wave band (fluctuation range). **c**, **d** denote the level of change in the duration (DUR) indicator, the red solid line represents the mean value of DUR over time, and the red area represents the wave band. **e**, **f** denote the level of change in the radiation range (RAR) indicator, the blue solid line represents the mean value of RAR over time, and the blue area represents the wave band.

and early warning during extreme weather events. The DAS-based monitoring systems could evolve into large-scale, terrestrial sensing networks to enable multi-dimensional and large-scale monitoring[40–43]. For example, leveraging a provincial network of 30 units could enable coordinated observations over extended regions, enhancing spatial coverage and monitoring accuracy. It is important to recognize the multi-factorial nature of natural disaster monitoring, as landslide disturbances are influenced by meteorological conditions (e.g., rainfall, wind speed), system configurations (e.g., cable installation, external interference), and other variables. Thus, effective real-time disturbance monitoring and timely anomaly alerts during extreme weather conditions necessitate a robust framework incorporating multidimensional signals characterization of spatiotemporal features and multivariate analysis.

Discussion

This study demonstrates the significant potential of DAS for high-resolution, real-time monitoring of landslide disturbances under extreme weather conditions. By analyzing DAS data captured during Super Typhoon Muifa, we successfully identified and characterized micro-deformation signatures associated with slope instability. The proposed spatiotemporal indicator framework based on SIG, DUR, and RAR proved effective in distinguishing landslide signals from ambient noise, offering a novel approach for dynamic hazard assessment. These contributions advance the capability for early detection and risk monitoring of rainfall-induced landslides in complex terrains. However, this study has not fully utilized large-scale data and has only verified feasibility. In terms of intelligent recognition, it is necessary to further introduce deep learning algorithms to achieve intelligent warning and identify symptomatic signals as early as possible. Future work could extend the application of DAS-based monitoring technology beyond observation, encompassing disaster assessment and forecasting for phenomena such as debris flows, earthquakes, and volcanic eruptions. The development of a unified, intelligent DAS-based monitoring system for natural disaster management holds promises for addressing pressing challenges in disaster risk reduction and environmental sustainability.

Methods

Raw data processing

The raw phase signals collected by the DAS system are inherently affected by various external noise sources, such as environmental vibrations, electromagnetic interference, and mechanical noise[44–46]. To effectively extract relevant information about landslide-induced disturbances under extreme weather conditions, it is essential to process these raw signals to minimize noise and enhance relevant signal features. In this study, we use downsampling to reduce the original high-frequency signal (2 kHz) to a lower frequency of 1 Hz. This downsampling allows for better alignment with the slower, large-scale movements associated with landslides and extreme

weather events while improving computational efficiency. We employ a low-pass filter to eliminate frequency components higher than half of the new sampling rate (0.5 Hz) and preserve the relevant low-frequency components of the signal. To further enhance the signal quality, we apply a variational mode decomposition (VMD) technique based on Pearson correlation coefficients[47]. VMD is a robust signal decomposition method that separates a complex signal into multiple intrinsic mode functions (IMFs), each representing different frequency components of the signal. This helps to reduce high-frequency noise, such as ambient vibrations and electromagnetic interference, that may remain after low-pass filtering. The resulting denoised signal exhibits an improved signal-to-noise ratio (SNR), increasing sensitivity to subtle changes in the disturbance signals induced by the Typhoon.

S-transform spectrum energy analysis

The S-transform, a hybrid time-frequency analysis method, is employed to analyze DAS signals associated with landslide disturbances[48,49]. This technique integrates the benefits of wavelet and short-time Fourier transforms, enabling localized spectrum decomposition with high temporal and frequency resolution. Its adaptability to non-stationary signals makes it particularly suitable for capturing the transient features inherent in landslide-induced vibrations. The transform preserves phase information and provides a continuous representation of signal energy across time and frequency domains. The S-transform is expressed as Eq. (2):

$$X_{DAS}(t,f) = \int_{-\infty}^{\infty} DAS_{\varepsilon}(\tau) \cdot g^{*}(\tau - t) \cdot e^{-j2\pi f(\tau - t)} d\tau \tag{2}$$

where $DAS(\tau)$ is the input signal, f is the frequency, τ is the time, and $g^{*}(\tau - t)$ is a Gaussian window function scaled by f. For appropriate window function types and parameters to match the signal characteristics and analysis requirements, we set the time window to 3600, the space window to 10, the overlap to half the window size, and the frequency range of 0–0.5 Hz.

To enhance temporal resolution, a sliding time window is employed, enabling the continuous monitoring of energy changes. This process allows the identification of abrupt energy progressive deformation in the time-frequency domain, corresponding to the initiation and evolution of landslide disturbances. The S-transform spectrum energy analysis provides a robust framework for detecting and characterizing landslide signals. By capturing localized, transient features, this method effectively leverages the high-resolution capabilities of DAS systems, offering critical insights into landslide dynamics under extreme environmental conditions.

Critical indicators for landslide monitoring

To effectively evaluate and quantify landslide hazard signals captured by the DAS system, we propose three key signal evaluation indicators to characterize the intensity of such events. These indicators are designed to leverage the unique capabilities of DAS in capturing high-resolution, continuous data across time and space dimensions.

Spectrum Intensity Gradient: The spectrum intensity gradient (SIG) measures the rate of change in signal power within the time-frequency domain and is pivotal for detecting sudden, transient events. By applying the S-transform over a sliding time window, we generate detailed spectrograms and compute the gradient of signal intensity over time, as shown in Eq. (3). This indicator effectively captures abrupt shifts in the time-frequency characteristics of the signal, such as sudden ground movements or precursors to slope failure. The SIG is particularly useful for real-time monitoring, as it highlights rapid, localized changes in subsurface activity. This capability underscores the feasibility of using DAS for early detection of landslides, as even subtle variations in micro-deformation noise can be systematically tracked to identify critical warning signs.

$$SIG_i(t,f) = \left| \frac{dX_{DAS_i}(t,f)}{dt} \right| \tag{3}$$

where $SIG_i(t,f)$ represents the SIG at time t and frequency f. $X_{DAS_i}(t,f)$ is the energy at time t and frequency f. According to the time-frequency map by S-transform, the gradient of energy spectrum intensity is calculated by difference, and the threshold is set to retain the effective gradient.

Duration: The duration (DUR) indicator quantifies the period over which the DAS signal maintains intensity above a defined threshold, representing sustained seismic or acoustic activity. This measure uses a Gaussian decay model to illustrate temporal attenuation of signal strength, capturing the duration of high-intensity phases[50]. The analysis of duration is significant for understanding the energy release and stability of the monitored terrain. During extreme weather conditions, where direct field observations and traditional sensors may become impractical or unsafe, the duration indicator derived from DAS data can continue to provide reliable information. By isolating these extended periods of activity, this indicator offers insights into the resilience of the landscape under prolonged stress, supporting rapid decision-making in risk-prone areas. We capture the effective range of high-intensity signals in the time dimension using sliding windows with a primary window size of 3600 s and a secondary window size of 600 s. The Gaussian decay model is established according to the mean and variance of the signal intensity in the window. The DUR of high-intensity signals is expressed as Eq. (4):

$$\begin{aligned} DUR_i &= T_w \cdot \sum_t \exp\left(-\frac{(t-t_0)^2}{2\sigma_i^2} \right) \cdot f(i,t), \\ f(i,t) &= \begin{cases} 1, & \text{if } \mathrm{X_{DAS,t}(i)} \geq \alpha \cdot \mathrm{X_{DAS_{max}}(i,t)} \\ 0, & \text{otherwise} \end{cases} \end{aligned} \tag{4}$$

where DUR_i denotes the duration for channel i, which quantifies the time length during which the energy of the signal remains above a certain threshold. T_w denotes the step size of the time secondary window. $X_{DAS,t}$ and $X_{DAS_{max}}$ represent the power at time t for channel i and the maximum power observed for channel i. These are the energy of the signal at a particular time point for the channel i and the baseline considered as a high-energy event. α is the threshold constant used to define what constitutes a "high energy" event. For example, setting $\alpha = 0.5$ means that the signal must exceed 50% of the maximum power at that channel to be considered significant. $f(i, t)$ represents the discriminant function that equals 1 when the power at time t for channel i exceeds the threshold, and 0 otherwise. This function effectively counts how many time steps the power remains above the threshold, contributing to the total duration.

Radiation range: The radiation range (RAR) describes disturbance propagation across monitoring zones, centered around high-gradient nodes identified by the spectrum intensity gradient. By applying a Gaussian decay model to these central nodes, we assess how the signal strength dissipates spatially across neighboring segments. This indicator allows for mapping the affected area, revealing energy radiation from the epicenter of activity and highlighting regions at greatest risk. The spatial analysis provided by this indicator demonstrates the ability of DAS to extend monitoring coverage over vast, continuous stretches of land, which is critical when extreme weather hampers access to remote or rugged terrains. This capability of DAS offers significant operational advantages compared to traditional point-based sensors, which may be vulnerable or difficult to maintain during severe weather. For the sliding window configuration of space dimension, we set the primary window to 1 km and the secondary window to 0.5 km according to the observation results. The spatial evolution of RAR in the energy spectrum is expressed as Eq. (5):

$$\begin{aligned} RAR_i &= S_w \cdot \sum_s \exp\left(-\frac{(s-s_0)^2}{2\sigma_s^2} \right) \cdot f(i,s), \\ f(i,s) &= \begin{cases} 1, & \text{if } \mathrm{X_{DAS,s}(i)} \geq \beta \cdot \mathrm{X_{DAS_{max}}(i,s)} \\ 0, & \text{otherwise} \end{cases} \end{aligned} \tag{5}$$

where RAR_i denotes the number of affected channels for channel i. S_w denotes the step size of the space secondary window. $X_{DAS,s}(i)$ and $X_{DAS_{max}}(i,s)$ represent the power at space window s for channel i and the

maximum intensity observed at channel i, used to normalize the energy levels. This represents the energy at a specific spatial point (channel s). The threshold constant β defines high energy in the space dimension (set to 0.5). The indicator function $f(i, s)$ equals 1 if the energy at channel s exceeds the threshold and 0 otherwise, indicating that channel s is affected by the high-energy event.

A sensitivity analysis confirms that the framework's output is robust within a practical threshold range. Lowering α and β increases the calculated DUR and RAR for confirmed events by classifying more marginal signal energy, thereby broadening the detected spatiotemporal area. Conversely, raising the thresholds confines the detection to only the most intense signal core, reducing DUR and RAR values. While these variations adjust the absolute magnitude of the indicators, the distinct spatiotemporal clusters corresponding to true landslides remain prominently identifiable against the background across thresholds, with non-landslide disturbances being effectively filtered out at higher values. This demonstrates a controllable trade-off between detection sensitivity and specificity and validates the selected threshold of 0.5 as a balanced baseline for our dataset. We therefore emphasize that these thresholds are best utilized as calibration parameters for operational deployment.

Data availability

The whole datasets of DAS, elevation and station generated in this study are available from the corresponding author on request. The 1Hz DAS signals and meteorological data used for analysis and generation in this study can be obtained from public data repositories at https://github.com/zhuchengyuan517/DAS-for-monitoring-landslides.git.

Code availability

The code and scripts used for signal processing in this study can be obtained from public data repositories at https://github.com/zhuchengyuan517/DAS-for-monitoring-landslides.git. The other codes used to generate the plots in this paper are available from the corresponding author on request.

Received: 19 November 2025; Accepted: 7 February 2026;
Published online: 27 February 2026

References

1. Stroth, A. & McDougall, S. Individual risk evaluation for landslides: key details. *Landslides* **19**, 977–991 (2022).
2. Shano, L., Raghuvanshi, T. K. & Meten, M. Landslide susceptibility evaluation and hazard zonation techniques–a review. *Geoenviron. Disasters* **7**, 1–19 (2020).
3. Dascher-Cousineau, K. & Bürgmann, R. Global subduction slow slip events and associated earthquakes. *Sci. Adv.* **10**, eado2191 (2024).
4. Lin, J. et al. Monitoring ocean currents during the passage of typhoon Muifa using optical-fiber distributed acoustic sensing. *Nat. Commun.* **15**, 1111 (2024).
5. Xie, T., Zhang, C.-C., Shi, B., Chen, Z. & Zhang, Y. Integrating distributed acoustic sensing and computer vision for real-time seismic location of landslides and rockfalls along linear infrastructure. *Landslides* **21**, 1941–1959 (2024).
6. Rodriguez, J. et al. Practical evaluation of single-frequency DGNSS for monitoring slow-moving landslides. *Landslides* **18**, 3671–3684 (2021).
7. Sarkawi, G. M. et al. Insights into tectonic hazards since the 2004 indian ocean earthquake and tsunami. *Nat. Rev. Earth Environ.* **6**, 17–34 (2025).
8. Materna, K. et al. Shallow slow slip events in the imperial valley with along-strike propagation. *Geophys. Res. Lett.* **51**, e2023GL108089 (2024).
9. Delbridge, B. G., Houston, H., Bürgmann, R., Kita, S. & Asano, Y. A weak subducting slab at intermediate depths below northeast japan. *Sci. Adv.* **10**, eadh2106 (2024).
10. Xiao, H. et al. Locating the precise sources of high-frequency microseisms using distributed acoustic sensing. *Geophys. Res. Lett.* **49**, e2022GL099292 (2022).
11. Handwerger, A. L., Huang, M.-H., Fielding, E. J., Booth, A. M. & Bürgmann, R. A shift from drought to extreme rainfall drives a stable landslide to catastrophic failure. *Sci. Rep.* **9**, 1569 (2019).
12. Panda, D. et al. Seasonal modulation of deep slow-slip and earthquakes on the main Himalayan thrust. *Nat. Commun.* **9**, 4140 (2018).
13. Handwerger, A. L. et al. Generating landslide density heatmaps for rapid detection using open-access satellite radar data in Google Earth Engine. *Nat. Hazards Earth Syst. Sci.* **22**, 753–773 (2022).
14. Hu, X., Bürgmann, R., Fielding, E. J. & Lee, H. Internal kinematics of the slumgullion landslide (USA) from high-resolution UAVSAR INSAR data. *Remote Sens. Environ.* **251**, 112057 (2020).
15. Jia, L., Wang, J., Gao, S., Fang, L. & Wang, D. Landslide risk evaluation method of open-pit mine based on numerical simulation of large deformation of landslide. *Sci. Rep.* **13**, 15410 (2023).
16. Hu, X., Bürgmann, R., Schulz, W. H. & Fielding, E. J. Four-dimensional surface motions of the slumgullion landslide and quantification of hydrometeorological forcing. *Nat. Commun.* **11**, 2792 (2020).
17. Zhan, Z. Distributed acoustic sensing turns fiber-optic cables into sensitive seismic antennas. *Seismol. Res. Lett.* **91**, 1–15 (2020).
18. Sladen, A. et al. Distributed sensing of earthquakes and ocean-solid earth interactions on seafloor telecom cables. *Nat. Commun.* **10**, 5777 (2019).
19. Williams, E. F. et al. Distributed sensing of microseisms and teleseisms with submarine dark fibers. *Nat. Commun.* **10**, 5778 (2019).
20. Biondi, E., Zhu, W., Li, J., Williams, E. F. & Zhan, Z. An upper-crust lid over the long valley magma chamber. *Sci. Adv.* **9**, eadi9878 (2023).
21. Michlmayr, G., Chalari, A., Clarke, A. & Or, D. Fiber-optic high-resolution acoustic emission (AE) monitoring of slope failure. *Landslides* **14**, 1139–1146 (2017).
22. Walter, F. et al. Distributed acoustic sensing of microseismic sources and wave propagation in glaciated terrain. *Nat. Commun.* **11**, 2436 (2020).
23. Li, J., Kim, T., Lapusta, N., Biondi, E. & Zhan, Z. The break of earthquake asperities imaged by distributed acoustic sensing. *Nature* **620**, 800–806 (2023).
24. Li, J.-T. et al. Coherently parallel fiber-optic distributed acoustic sensing using dual Kerr soliton microcombs. *Sci. Adv.* **10**, eadf8666 (2024).
25. Xiao, H., Spica, Z. J., Li, J. & Zhan, Z. Detection of earthquake infragravity and tsunami waves with underwater distributed acoustic sensing. *Geophys. Res. Lett.* **51**, e2023GL106767 (2024).
26. Lindsey, N. J., Dawe, T. C. & Ajo-Franklin, J. B. Illuminating seafloor faults and ocean dynamics with dark fiber distributed acoustic sensing. *Science* **366**, 1103–1107 (2019).
27. Zhu, W., Allison, K. L., Dunham, E. M. & Yang, Y. Fault valving and pore pressure evolution in simulations of earthquake sequences and aseismic slip. *Nat. Commun.* **11**, 4833 (2020).
28. Mousavi, S. M., Ellsworth, W. L., Zhu, W., Chuang, L. Y. & Beroza, G. C. Earthquake transformer-an attentive deep-learning model for simultaneous earthquake detection and phase picking. *Nat. Commun.* **11**, 3952 (2020).
29. Yang, L., Liu, X., Zhu, W., Zhao, L. & Beroza, G. C. Toward improved urban earthquake monitoring through deep-learning-based noise suppression. *Sci. Adv.* **8**, eabl3564 (2022).
30. Ouellet, S. M. et al. Previously hidden landslide processes revealed using distributed acoustic sensing with nanostrain-rate sensitivity. *Nat. Commun.* **15**, 6239 (2024).
31. Dai, K. et al. Entering the era of earth observation-based landslide warning systems: a novel and exciting framework. *IEEE Geosci. Remote Sens. Mag.* **8**, 136–153 (2020).
32. Muñoz, F. & Soto, M. A. Enhancing fibre-optic distributed acoustic sensing capabilities with blind near-field array signal processing. *Nat. Commun.* **13**, 4019 (2022).
33. Lin, Q. et al. Evaluation of potential changes in landslide susceptibility and landslide occurrence frequency in China under climate change. *Sci. Total Environ.* **850**, 158049 (2022).

34. Fang, G., Li, Y. E., Zhao, Y. & Martin, E. R. Urban near-surface seismic monitoring using distributed acoustic sensing. *Geophys. Res. Lett.* **47**, e2019GL086115 (2020).
35. Yu, C., Zhan, Z., Lindsey, N. J., Ajo-Franklin, J. B. & Robertson, M. The potential of das in teleseismic studies: insights from the goldstone experiment. *Geophys. Res. Lett.* **46**, 1320–1328 (2019).
36. Atterholt, J., Zhan, Z. & Yang, Y. Fault zone imaging with distributed acoustic sensing: Body-to-surface wave scattering. *J. Geophys. Res. Solid Earth* **127**, e2022JB025052 (2022).
37. Karrenbach, M. et al. Fiber-optic distributed acoustic sensing of microseismicity, strain and temperature during hydraulic fracturing. *Geophysics* **84**, D11–D23 (2019).
38. Jousset, P. et al. Dynamic strain determination using fibre-optic cables allows imaging of seismological and structural features. *Nat. Commun.* **9**, 2509 (2018).
39. Yoshihara, F., Harrabi, K., Niskanen, A., Nakamura, Y. & Tsai, J. S. Decoherence of flux qubits due to 1/f flux noise. *Phys. Rev. Lett.* **97**, 167001 (2006).
40. Li, J., Zhu, W., Biondi, E. & Zhan, Z. Earthquake focal mechanisms with distributed acoustic sensing. *Nat. Commun.* **14**, 4181 (2023).
41. Jousset, P. et al. Fibre optic distributed acoustic sensing of volcanic events. *Nat. Commun.* **13**, 1753 (2022).
42. Zhu, W. et al. Seismic arrival-time picking on distributed acoustic sensing data using semi-supervised learning. *Nat. Commun.* **14**, 8192 (2023).
43. Nishimura, T. et al. Source location of volcanic earthquakes and subsurface characterization using fiber-optic cable and distributed acoustic sensing system. *Sci. Rep.* **11**, 6319 (2021).
44. Tsuji, T., Tsuji, S., Kinoshita, J., Ikeda, T. & Ahmad, A. B. 4 cm portable active seismic source (pass) for meter-to kilometer-scale imaging and monitoring of subsurface structures. *Seismol. Soc. Am.* **94**, 149–158 (2023).
45. Zhu, C., Pu, Y., Yang, K., Yang, Q. & Chen, C. P. Distributed optical fiber intrusion detection by image encoding and swint in multi-interference environment of long-distance pipeline. *IEEE Trans. Instrum. Meas.* **72**, 1–12 (2023).
46. Yang, Y., Zhang, H. & Li, Y. Long-distance pipeline safety early warning: a distributed optical fiber sensing semi-supervised learning method. *IEEE Sens. J.* **21**, 19453–19461 (2021).
47. Zhu, C., Pu, Y., Lyu, Z., Yang, K. & Yang, Q. Multidimensional information fusion and broad learning system-based condition recognition for energy pipeline safety. *Knowl. Based Syst.* **300**, 112259 (2024).
48. Wu, S., Wang, Y. & Liang, X. Time-delay estimation of microseismic DAS data using band-limited phase-only correlation. *IEEE Trans. Geosci. Remote Sens.* **61**, 1–9 (2022).
49. Liu, B., Liu, Q. & Kang, X. Application of improved time–frequency representation to local noise removal. *J. Pet. Explor. Prod. Technol.* **11**, 2091–2096 (2021).
50. Bloch, I., Hänsch, T. W. & Esslinger, T. Measurement of the spatial coherence of a trapped Bose gas at the phase transition. *Nature* **403**, 166–170 (2000).

Acknowledgements

The authors thank Roland Burgmann for his guidance and assistance in the later stages of this research. This work is supported by the Yangtze River Delta Science and Technology Innovation Community Joint Research (Key Challenge Tasks) Project (20259b09050007), National Key R&D Program of China (2021YFD1400200), Baima Lake Laboratory Joint Funds of the Zhejiang Provincial Natural Science Foundation of China (LBMHD24F030001).

Author contributions

C.Z. and W.Z. wrote the main manuscript text, Y.Y. wrote and edited the manuscript, Q.Y. and K.Y. investigated the feasibility of the research, and Q.Y. supervised, verified, and provided funding for the research. All authors reviewed the manuscript.

Competing interests

The authors declare no competing interests.

Additional information

Supplementary information The online version contains supplementary material available at https://doi.org/10.1038/s44304-026-00182-y.

Correspondence and requests for materials should be addressed to Kaixiang Yang or Qinmin Yang.